Infrared Cloud Imager Development for Atmospheric Optical Communication Characterization, and Measurements at the JPL Table Mountain Facility

Paul W. Nugent,* Joseph A. Shaw,* and Sabino Piazzolla†

ABSTRACT. — The continuous demand for high data return in deep space and near-Earth satellite missions has led NASA and international institutions to consider alternative technologies for high-data-rate communications. One solution is the establishment of wide-bandwidth Earth–space optical communication links, which require (among other things) a nearly obstruction-free atmospheric path. Considering the atmospheric channel, the most common and most apparent impairments on Earth–space optical communication paths arise from clouds. Therefore, the characterization of the statistical behavior of cloud coverage for optical communication ground station candidate sites is of vital importance. In this article, we describe the development and deployment of a ground-based, long-wavelength infrared cloud imaging system able to monitor and characterize the cloud coverage. This system is based on a commercially available camera with a 62-deg diagonal field of view. A novel internal-shutter-based calibration technique allows radiometric calibration of the camera, which operates without a thermoelectric cooler. This cloud imaging system provides continuous day–night cloud detection with constant sensitivity. The cloud imaging system also includes data-processing algorithms that calculate and remove atmospheric emission to isolate cloud signatures, and enable classification of clouds according to their optical attenuation. Measurements of long-wavelength infrared cloud radiance are used to retrieve the optical attenuation (cloud optical depth due to absorption and scattering) in the wavelength range of interest from visible to near-infrared, where the cloud attenuation is quite constant. This article addresses the specifics of the operation, calibration, and data processing of the imaging system that was deployed at the NASA/JPL Table Mountain Facility (TMF) in California. Data are reported from July 2008 to July 2010. These data describe seasonal variability in cloud cover at the TMF site, with cloud amount (percentage of cloudy pixels) peaking at just over 51 percent during February, of which more than 60 percent had optical attenuation exceeding 12 dB at wavelengths in the range from the visible to the near-infrared. The lowest cloud amount was found during August, averaging 19.6 percent, and these clouds were mostly optically thin, with low attenuation.

* Electrical and Computer Engineering Department, Montana State University, Bozeman, Montana.
† Communications Architectures and Research Section.

The research described in this publication was carried out by the Jet Propulsion Laboratory, California Institute of Technology, under a contract with the National Aeronautics and Space Administration.

I. Introduction

The demand for high-data-rate communication is generating interest in Earth–space optical links as an alternative or extension to radio-based links [1–3], and the establishment of such links to both near-Earth and deep-space platforms is being pursued. Testament to this interest in optical communications are future NASA missions such as the Lunar Laser Communications Demonstration (LLCD) and Laser Communications Relay Demonstration (LCRD), which will involve optical links from a spacecraft orbiting the Moon [4] and an optical terminal aboard a geostationary (GEO) satellite [5].

One of the key parameters of concern for an Earth–space optical communication link is cloud cover at the ground station [3], which manifests itself in different fashions. Thin clouds attenuate the optical signal, based on their optical properties [6]. Optically thick clouds completely break the communication link. Improvement of the cloud-impaired link availability can be obtained through the use of multiple ground stations located at carefully selected sites (site diversity) [3]. Optimal use of site diversity requires that the local cloud cover between sites be statistically independent, or preferably anticorrelated [3]. Proper site selection, therefore, requires knowledge of the long-term cloud cover correlations between each site, with high temporal and spatial resolutions.

There are several approaches to obtaining cloud cover data for the statistical description of potential optical ground station sites. Surface observations, for instance, may provide long-term information of cloud coverage for a number of specific sites in the United States and the world [3]. Surface observation data, however, are generally available for sites close to airports or urban centers, which are not the high-elevation locations preferred for ground-station telescopes. Satellite imagery can provide worldwide cloud coverage data [7] but with a trade-off between spatial and temporal resolution. Satellites in geosynchronous orbit provide continuous data, but at low spatial resolution, and satellites in near-Earth orbits provide higher spatial resolution, but only once or twice per day. Moreover, for all these methods it is to difficult detect the presence and the effects of thin clouds.

In this article, we present an alternate approach of developing and deploying an infrared cloud imager to measure cloud signatures for the statistical representation of cloud coverage. The cloud imager has been deployed at the NASA/JPL Table Mountain Facility (TMF) in California, which houses a number of telescopes including the Optical Communications Telescope Laboratory (OCTL), which is dedicated to optical communications [8]. The cloud imager was made using commercial-off-the-shelf (COTS) parts and custom software. The camera is sensitive in the long-wavelength infrared (LWIR) spectrum, and therefore is able to detect the presence of clouds in daytime and nighttime using a consistent detection method with a consistent sensitivity. The rest of the article is organized as follows. First, the development of the cloud imager is described. Then, the process for isolating the cloud signature, including the corrections necessary to remove extraneous readings, such as the emission from the germanium window of the weatherproof enclosure, are discussed. Finally, the statistical results of two years' of data collection at TMF are presented.

II. The Second-Generation Infrared Cloud Imager (ICI2) at Table Mountain

The ideal instrument to measure cloud cover on Earth–space optical channels would provide continuous data day and night with high spatial and temporal resolution, and would classify clouds by their expected optical attenuation. Also, in an ideal situation, the instrument should produce a real-time cloud product. Finally, the cloud imager should be an autonomous instrument able to function without human supervision and capable of operating in all possible weather conditions. The need for an instrument that meets these requirements led to collaboration between the JPL Optical Communications Group and Montana State University (MSU). This collaboration focused on the development of a relatively low-cost cloud imager based on the Infrared Cloud Imager (ICI), an instrument developed to measure long-term cloud statistics for climate studies [9,10].

The ICI systems are ground-based LWIR imagers that image the sky, remove the atmospheric emission, and process the remaining signal to provide cloud detection and classification [9–12]. Ground-based thermal imaging for cloud detection has advantages over traditional methods. For example, satellites achieve spatial resolutions between 1 km and tens of kilometers per pixel for cloud detection [13,14], sometimes insufficient to characterize local variability. ICI systems operate continuously day and night with a constant sensitivity. Other systems, based on visible wavelengths, may provide high spatial and temporal resolution in daylight [15], and when they can operate at night they do so with reduced sensitivity relative to their daytime cloud detection [16]. LWIR cloud imagers instead detect the thermal emission of the sky and therefore provide continuous cloud measurements of high spatial and temporal resolution in a manner not available from other systems.

The cloud imager described in this article is named the second-generation Infrared Cloud Imager (ICI2). The idea for the ICI2 was to have a radiometrically calibrated LWIR imaging system, with stable internal calibration achieved without use of onboard or external blackbody calibration sources, housed in a simple weatherproof enclosure with an optical window rather than a moving hatch for continuous outdoor deployment. The ICI2 uses a FLIR Systems, Inc., Photon 320 LWIR camera, shown in Figure 1. This camera has an uncooled 324×256 pixel microbolometer focal plane array (FPA), which operates without a thermo-

Figure 1. Photograph of the Photon core camera used in the ICI2.

electric cooler element (the pixel numbering is shown along the borders of a number of the infrared images in this article). In the ICI2 at TMF, a 14.25-mm-focal-length lens provides a 62-deg diagonal field of view (FOV), or an instantaneous horizontal FOV of 0.14 deg per pixel.

The Photon 320 has maximum response from 7.5 μm to 13.5 μm, within the approximately 8–14 μm atmospheric window. This spectral region is well suited for ground-based cloud detection because of the low absorption and emission of the atmosphere and the relatively high emission from clouds (see Section III.C).

To house the camera and associated electronics, an environmentally sealed steel enclosure is used, as shown in Figure 2. The camera views the sky through a diamond-coated germanium window, with a baffle between the lens and germanium window to reduce stray light. A heater inside the enclosure keeps the system at stable temperature during cold weather while a fan circulates the internal air. Camera data are available through a 14-bit digital low-voltage digital signaling (LVDS) channel that is read by a computer through an LVDS-to-Ethernet module. This module also provides an RS-232-over-Ethernet channel that is used for camera control.

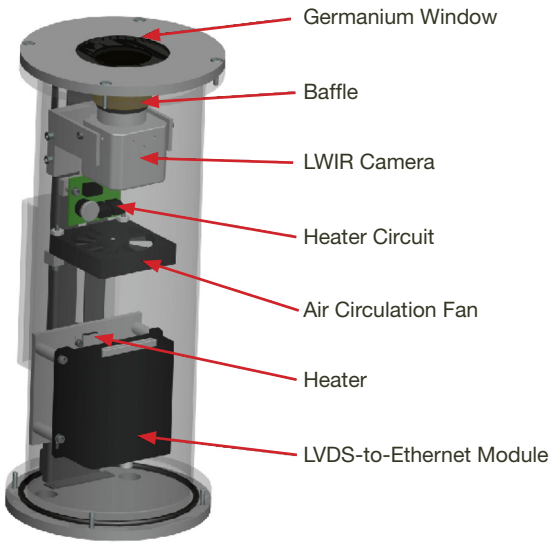

Figure 2. The compact ICI2 system in its environmental enclosure with a germanium window.

After initial conception in a collaboration between JPL and MSU, the ICI2 system development, characterization, and testing took place at MSU in Bozeman, Montana, and at JPL TMF [11,12,17]. The system was permanently deployed at TMF in July 2008, and it continues to run up to the present time. This article gives an overview of the ICI2 system, describes the cloud detection and classification techniques, and demonstrates the capabilities of the ICI2 for providing continuous day/night detection and classification of clouds with data from TMF from July 2008 to July 2010.

III. ICI2 Data Processing

The ICI2 is not only a cloud imager, but a quite sophisticated cloud detection/image processing system. Sky images from the ICI2 are processed to isolate clouds from the background atmosphere [9,11]. First, the data (images) are calibrated to represent integrated sky radiance (due to clouds plus atmospheric emission). Then, atmospheric emission models are used to calculate and remove atmospheric emission from the images. Thresholds are then applied to the images to detect clouds from the remaining residual radiance. This technique has proven reliable through past deployments of ICI systems and comparisons with other co-located instruments, including microwave radiometers, cloud lidars, cloud radars, and visible-wavelength cloud imagers [9,10]. The ICI2 extends this technique to classify clouds according to their optical depth (OD) and corresponding attenuation (due to cloud absorption and scattering) [12] in the wavelength range from the visible to the near-infrared (explained in Section III.E). Figure 3 shows an example of the ICI2 processed data. The downwelling sky radiance image, Figure 3(a), has been processed to give the cloud attenuation image in Figure 3(b). A diagram of the data processing technique that produces these images is shown in Figure 4, where each step has been labeled to correspond to a subsection of this article.

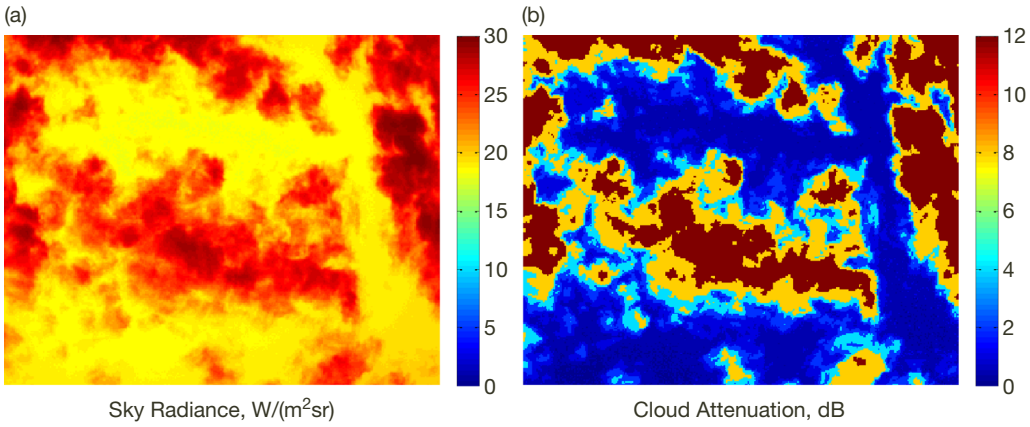

Figure 3. A sample cloud product from the ICI2 at TMF showing (a) the sky radiance, and (b) cloud attenuation, using data collected on October 2, 2008 at 5:50 UTC. Cloud attenuation is referred to the wavelength range from the visible to the near-infrared.

A. Radiometric Calibration of the ICI2 Data

The first step of ICI2 data processing is radiometric calibration of the image. Calibration allows the atmospheric emission to be removed to isolate the cloud emission [9,10]. The calibration is performed in terms of scene radiance rather than temperature because the response of a microbolometer camera is linear with radiance, and, therefore, subtraction of atmospheric emission is more easily performed with radiance rather than temperature. Furthermore, because each microbolometer pixel can have a quite different response, the calibration must be calculated with matrices that represent the gain and offset terms of a linear calibration equation that relates scene radiance to detector output, individually for each pixel.

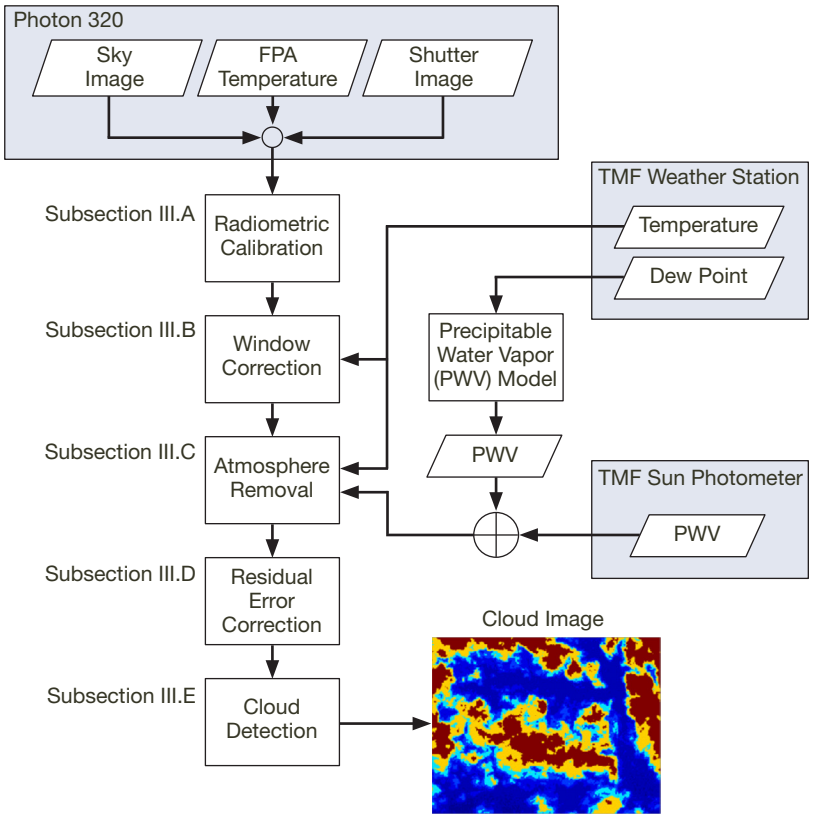

Figure 4. Flow diagram for the data processing algorithm used to process ICI2 sky images to derive cloud detection and cloud attenuation images at TMF.

The ICI2 Calibration Process

The main issue for a microbolometer FPA without thermal stabilization, such as the one used for the Photon camera, is that the response of each pixel depends on its temperature, and therefore a procedure is necessary to calibrate the FPA detector readings for changes in FPA temperature. To correct for errors caused by changes in the FPA temperature, the ICI2 was located in a thermal chamber and the temperature of the camera was varied while the camera viewed a constant blackbody source. Then, this cycle was repeated over a set of blackbody reference images. In this way, the dependence of the camera response with variable FPA temperature was characterized. Moreover, images of the closed shutter were used as an equivalent calibration source to correct for changes in the camera offset [11,17].

Figure 5 shows a diagram of the ICI2 calibration procedure. Data are collected and calibrated in the following manner:

(1) A nonuniformity correction is performed to achieve a spatially constant response for all pixels (a process also termed “flat fielding”).

(2) An image of the scene is recorded along with the current FPA temperature.

(3) The shutter of the camera is closed and an image of the shutter is collected, along with the current FPA temperature (which is used as the shutter temperature).

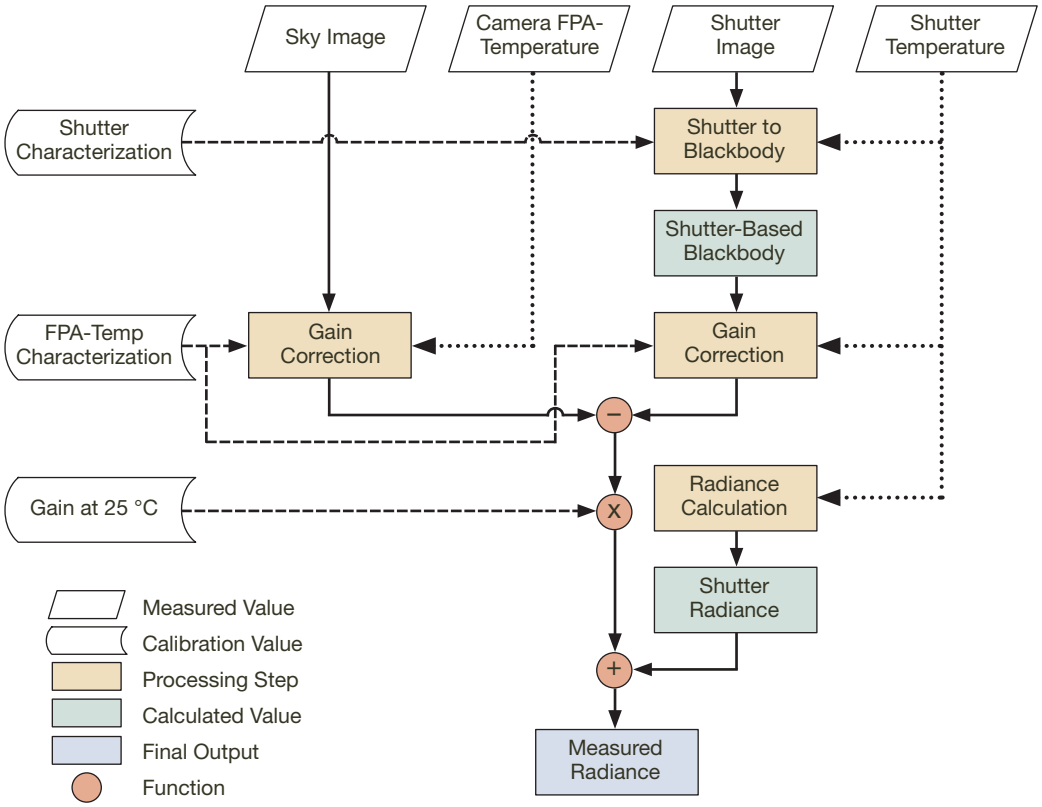

Figure 5. Diagram of the ICI2 radiometric calibration process.

(4) The shutter image is scaled by a function that converts an image of the shutter to an equivalent image of a blackbody outside the camera at the FPA temperature. The scene image and the shutter-based blackbody images are corrected for the FPA-temperature-dependent response (referenced to an FPA temperature of 25 deg C). The difference between these images is determined, and is multiplied by the gain of the camera calculated for an FPA temperature of 25 deg C. The radiance of a blackbody at the shutter temperature is added to produce a radiometric image of the scene. This technique produces radiance images with an uncertainty of ±0.45 W/(m^2 sr) in the reading of the integrated radiance at each pixel.

B. Correcting for the Germanium Window

Because the ICI2 is protected by a weatherproof enclosure with a diamond-coated germanium window that has high transmittance in the LWIR (approximately 0.85), the optical effects of this window must be estimated and removed before clouds can be identified. The components of the signal observed by the camera behind the germanium window are described in Figure 6. The measured signal L_m is the sum of the desired scene radiance L_s multiplied by the band-averaged window transmittance τ_w, the unwanted radiance emitted inside the enclosure L_e multiplied by the band-averaged window reflectance ρ_w, and the unwanted radiance emitted by the germanium window L_w:

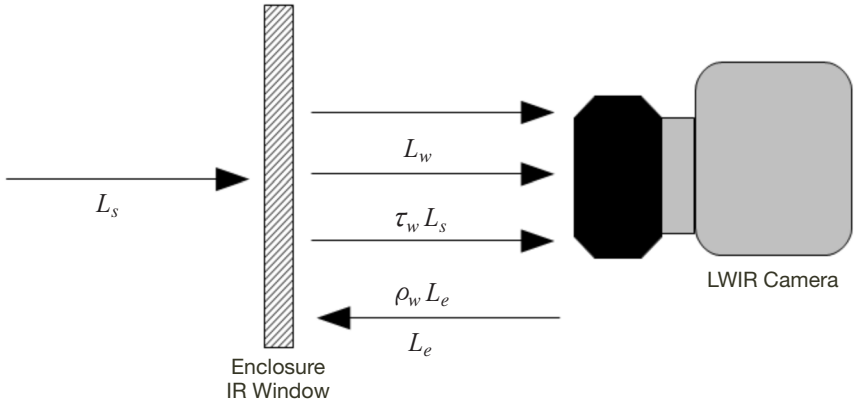

Figure 6. Diagram of an infrared camera behind an IR window. The signal measured by the camera depends on factors that include scene radiance (L_s), window transmittance (τ_w), window reflectance (ρ_w), thermal emission from inside the enclosure (L_e), and thermal emission from the window (L_w).

$$L_m = \tau_w L_s + \rho_w L_e + L_w \tag{1}$$

Solving for L_s yields

$$L_s = \frac{L_m - \rho_w L_e - \varepsilon_w L_{wbb}}{\tau_w} = \frac{1}{\tau_w} L_m - \frac{\rho_w}{\tau_w} L_e - \frac{\varepsilon_w}{\tau_w} L_{wbb} \tag{2}$$

With sufficient information, the signal measured behind the window can be corrected to give a measurement of the sky as observed outside the window. In the ICI2, the emission from inside the enclosure L_e is calculated as blackbody radiation at the camera temperature, and the window radiance L_w is determined as a graybody at the window temperature with emissivity ε_w. The values of τ_w, ρ_w, and ε_w were characterized during an initial deployment of the ICI2 at MSU [18]. In these experiments, the ICI2 was operated beside another calibrated cloud imager that operated without a germanium window. The simultaneous data from the two imagers were used to derive an angle-dependent model of the window parameters $\tau_w(\theta)$, $\rho_w(\theta)$, and $\varepsilon_w(\theta)$, where θ is the zenith angle of each pixel. The angle dependence is shown as a fifth-order polynomial in Figure 7.

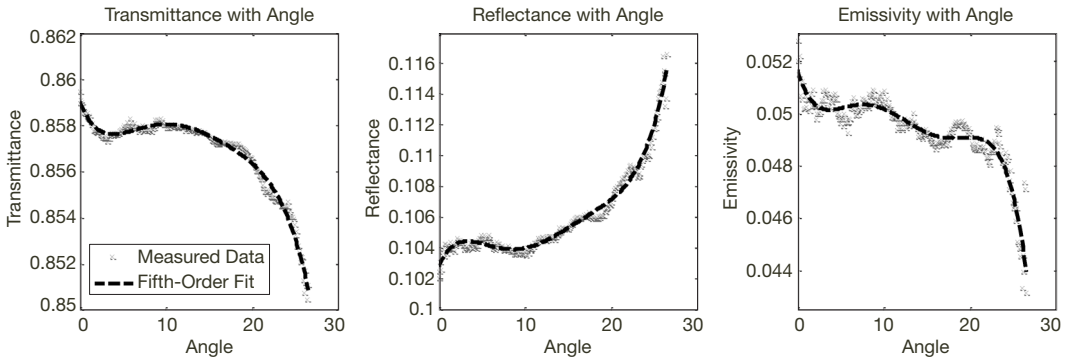

Figure 7. Window parameters $\tau_w(\theta)$, $\rho_w(\theta)$, and $\varepsilon_w(\theta)$: τ_w varies from 0.850 to 0.859, with an average of 0.857; ρ_w varies from 0.102 to 0.116, with an average of 0.106; ε_w varies from 0.043 to 0.053, with an average of 0.050.

Examples of uncorrected and corrected images from the JPL ICI2 system are shown in Figure 8, alongside a simultaneous image from the MSU ICI2 system that operated without a window. The correction reduced the difference between the co-located imagers from 4.9 W/(m^2 sr) to 0.77 W/(m^2 sr). Accounting for the calibration uncertainty of ±0.45 W/(m^2 sr) for each camera, the uncertainty of the ICI2 with the window can be estimated as ±0.65 W/(m^2 sr). This accuracy limits the minimum cloud detection level achievable with the ICI2 system. Detection levels are addressed in Section III.E. Complete details of the window correction process are available elsewhere [18].

Figure 8. Cloud-detection images from two cloud imagers taken at 11:37 MDT (UTC–6), April 29, 2008. The image panels (left to right) show cloud maps from the cloud imager system (MSU-ICI2) with no window, the uncorrected JPL-ICI2 system with the window, and the corrected JPL-ICI2 system.

C. Removal of Atmospheric Emission

The 8–14 μm spectral band is referred to as the LWIR atmospheric window. This is an ideal spectrum for continuous cloud detection because of high atmospheric transmission, low atmospheric emission, and relatively high cloud emission. To better illustrate this concept, Figures 9 and 10 illustrate the atmospheric windows in this spectrum according to simulations obtained using MODTRAN atmospheric radiative transfer software [19]. Figure 9 shows a transmittance spectrum of the atmosphere for a zenith path to space through the use of the "1976 U.S. Standard Atmosphere" [20] for an elevation of 2.2 km above sea level (ASL), which is representative of Table Mountain, California. The simulation was run for two water vapor profiles: the default US76 profile (black line) and the default profile with 1.5 times higher water vapor content (red line). Figure 10 shows downwelling clear-sky emission for these two atmospheric models: default US76 (black), and US76 with 1.5 times water vapor (red). Figure 11 describes the downwelling spectral radiance when clouds have been added to the US76 atmosphere. In this figure, clear-sky downwelling emission is plotted along with emission spectra for three cloud types: optically thin cirrus clouds at 10 km above mean sea level, MSL (1 km thick, 550-nm OD = 0.25); cirrus clouds at 10 km MSL (1 km thick, 550-nm OD = 1); and optically opaque altostratus clouds at 4.7 km MSL (0.6 km thick). The emission peak and transmission dip at 9.6 μm are both consequences of ozone (O_3) in the stratosphere.

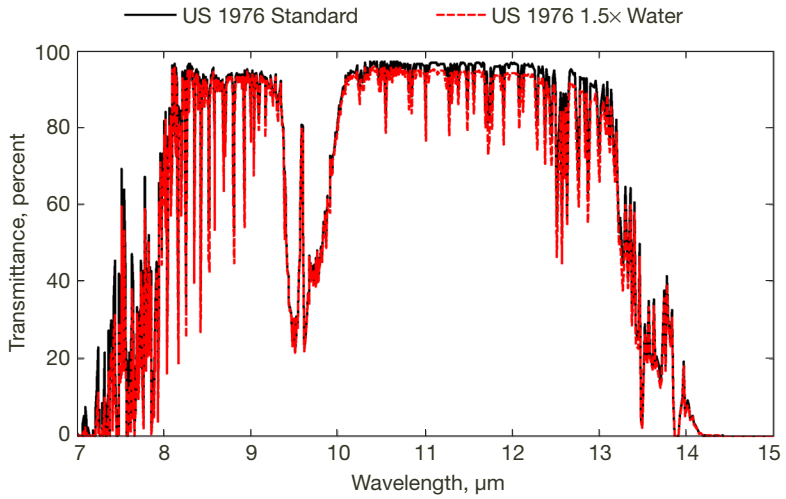

Figure 9. Simulated transmittance for the US76 atmosphere (ground level 2.29 km ASL) with water vapor profiles using default (black) and 1.5 times default (red) values.

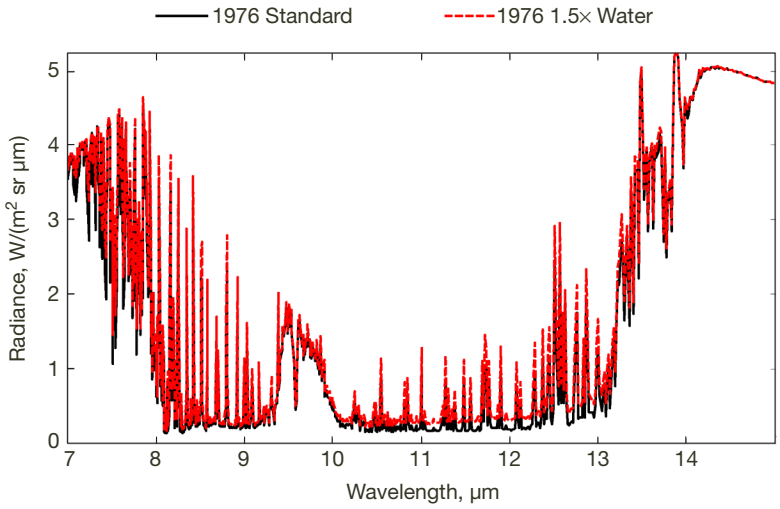

Figure 10. Downwelling atmospheric emission spectra for US76 atmosphere with 1.5 times default water vapor (red, top), and US76 atmosphere (black, bottom).

Emission in the 8–14 μm band depends on atmospheric conditions and clouds as follows:

(1) Clear-sky emission arises largely from water vapor, and increases with increased water vapor content.

(2) Cloud emission depends on the cloud optical depth and altitude.

(3) Optically thick clouds have high emission and can be detected easily.

(4) Optically thin clouds, typically at higher altitudes and colder temperatures, have lower emission.

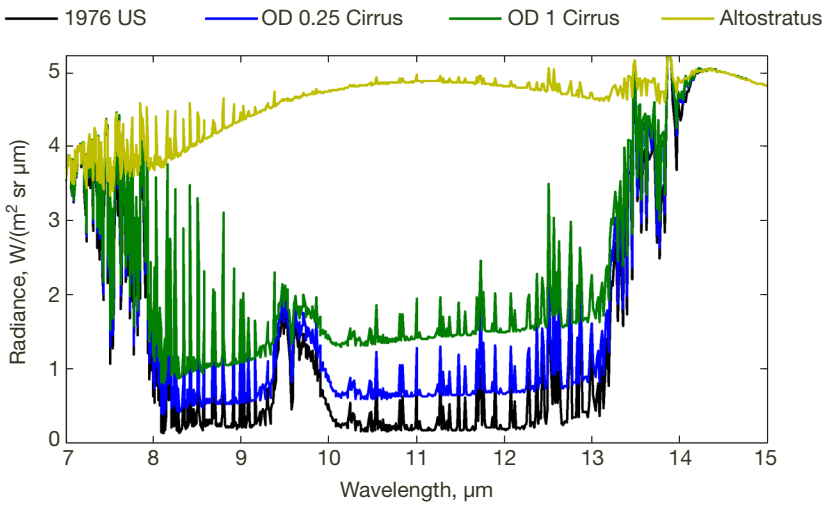

Figure 11. Downwelling emission from a cloudy and clear atmosphere: altostratus at 3.9 km MSL (gold, top), OD 1 cirrus at 10 km MSL (green, middle), OD 0.25 cirrus at 10 km (blue, second from bottom), and clear sky (black, bottom).

Any thermal infrared measurement includes emission of the clear atmosphere and clouds if present; therefore, detection (and isolation) of the cloud emission requires knowledge and careful removal of the atmospheric emission from the initial measurement.

Atmospheric emission in the thermal infrared can be derived from the profile of water vapor and temperature along the atmospheric path. At TMF, these profiles are available from radiosondes but these launches do not occur often enough to characterize the changing atmospheric background. Therefore, an emission model was used to estimate atmospheric emission using surface measurements of precipitable water vapor, near-surface air temperature, and dew point temperature.

ICI2 Atmospheric Radiance Models

To develop the TMF atmospheric radiance model, MODTRAN simulations were run using vertical profiles of atmospheric pressure, temperature, and humidity measured by radiosondes launched from TMF between January 2006 and December 2008. These profiles provided a variety of air temperatures and water vapor levels. To further vary the water vapor information in each profile, the water vapor content was scaled in the simulations to produce precipitable water vapor content from 0.01 cm to saturation (approximately 2.5 cm or less). To account for increased emission with zenith angle, each atmosphere and water vapor increment was simulated at zenith angles from zero to 40 deg in 5-deg steps. Simulated data are shown for a zenith angle of 0 deg in Figure 12(a) and 40 deg in Figure 12(b). These data were used to derive a model that relates the band-integrated sky radiance to surface temperature, precipitable water vapor W_p, and zenith angle. The resulting model is shown in Equation 3.

$$L_{sky} = L_s W_p A + W_p B + L_s C + D \tag{3}$$

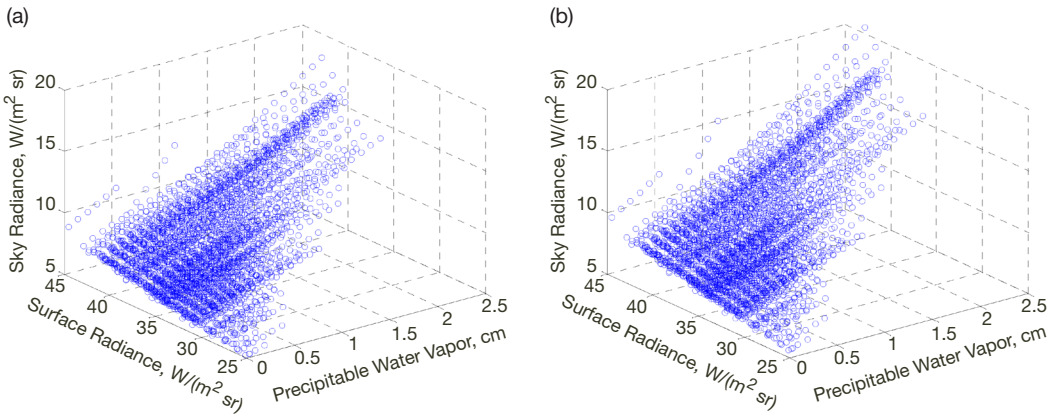

Figure 12. Atmospheric emitted radiance (L_{sky}) plotted as a function of surface radiance (blackbody radiance at the air temperature, L_s), and precipitable water vapor for zenith angles of (a) 0 deg and (b) 40 deg.

In Equation (3), L_{sky} is the clear-sky radiance, L_s is the radiance for a blackbody at the temperature of the near-surface air (measured by the TMF weather station), and W_p is the precipitable water vapor column in cm. Precipitable water vapor data at TMF were acquired from the TMF Sun photometer station when available or otherwise estimated (described later). The coefficients A, B, C, and D are derived from a 2D linear regression at each zenith angle. These coefficients are shown in Figure 13. A spline interpolation is used to determine these coefficients at all angles throughout the ICI2's FOV. These angle-dependent coefficients are then used to determine a modeled clear-sky image that is removed from the calibrated sky radiance image to produce a residual radiance image.

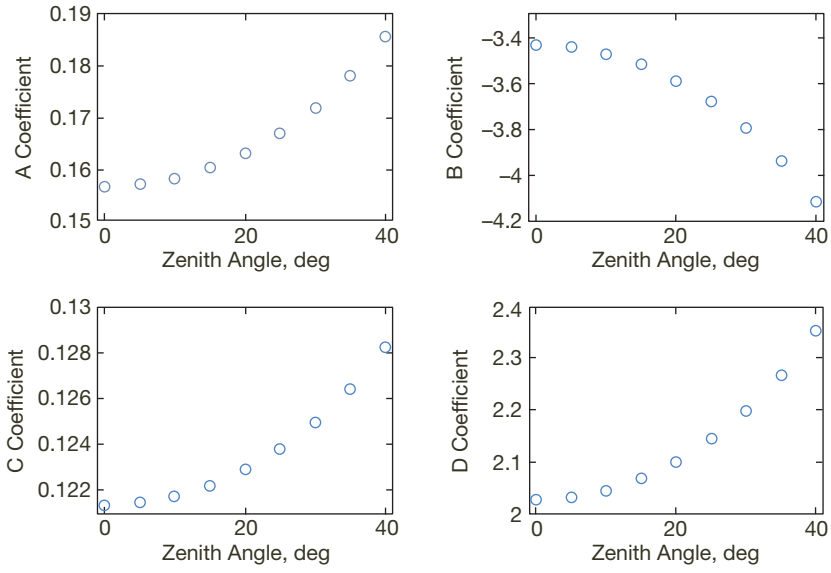

Figure 13. The coefficient of the TMF atmosphere radiance model calculated for zenith angles from 0 deg to 40 deg. During operation, a spline interpolation is used to determine the coefficient for each pixel across the ICI2's FOV using the measured zenith angle of each pixel.

Precipitable Water Vapor at TMF

Measurements of precipitable water vapor (W_p) at TMF are available periodically from a resident Sun photometer that is part of the Aerosol Robotic Network (AERONET) operated by NASA [21]. This instrument provides precipitable water vapor measurements when a cloud-free path to the Sun is available. Therefore, temporal gaps in the precipitable water vapor data exist during the night and periods of cloudy skies. These gaps are filled using the Reitan relationship model, which estimates precipitable water vapor from measurements of the surface dew point [22]. This relationship relates the natural logarithm of the precipitable water vapor to a linear function of the surface dew point:

$$\ln(W_p) = aT_{dew} + b, \tag{4}$$

where T_{dew} is the dew point temperature (in kelvins) and a and b are coefficients specific to the location of interest. A Reitan model specific for TMF was derived using W_p data from radiosondes launched at TMF and from the TMF Sun photometer, along with dew point measurements from the TMF weather station. Figure 14 shows these data with the Reitan model for each data set. A least-squares fit to these data was used to derive the coefficients a and b in Equation 5:

$$\ln(W_p) = 0.074T_{dew} - 20.69. \tag{5}$$

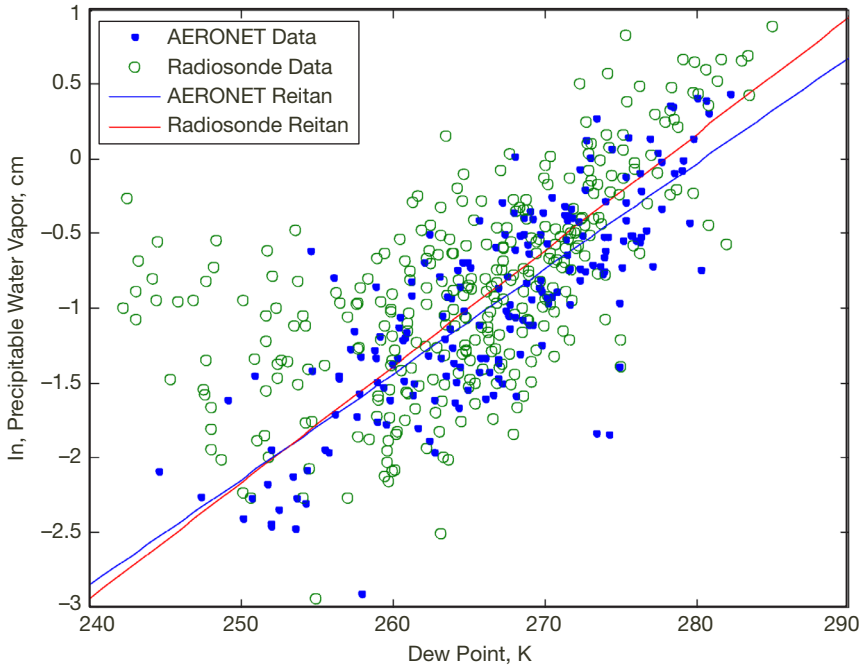

Figure 14. The natural logarithm of precipitable water vapor data from AERONET (dots) and radiosonde (circles) are plotted against surface dew-point temperature. Reitan linear functions (Equation [4]) according to the Sun photometer data (blue) and radiosonde data (red) are shown.

To summarize, the data processing of the ICI2 system uses Sun photometer precipitable water vapor data when available and a Reitan model to fill in the gaps. In this model, bounding Sun photometer data points are used to update the slope of the model, assuming the slope changes linearly over time. This procedure has been shown to improve the Reitan water vapor estimation [23], and is particularly valuable during the night when no Sun photometer data are available.

Adaptive Atmosphere Radiance Removal

As discussed earlier, the sky radiance measured by the ICI2 is affected by the emission, reflection, and transmission of the germanium window and the emission from the atmosphere. Therefore, the ICI2 data processing requires highly accurate window correction and water vapor estimation. Although great care is taken to correct for the window and to estimate the atmospheric water vapor content, these routines are not perfect and their uncertainties reduce the accuracy of the ICI2. There are also sources of error, such as temperature inversions where the near-surface air temperature does not accurately reflect the low-level atmospheric temperature and solar scattering off optical elements in the camera, which cause a variable background that cannot be characterized readily. Therefore, an adaptive algorithm was developed that allows the atmosphere radiance models to be adjusted to fit current conditions, thereby reducing the uncertainty in the measurements.

The approach behind this method is to detect clear-sky regions in the sky mapped by the imager, calculate the atmospheric emission associated with this clear-sky region, and then use the ratio between the measured and calculated emissions to subtract a properly scaled radiance from the emission in other regions of the sky. Clear skies are detected using three criteria:

(1) Regions that closely match the angular gradient of the modeled clear-sky radiance. This criterion locates regions of likely clear sky where the gradient closely matches the expected $\sec(\phi_z)$ dependence.

(2) Regions that do not exceed the modeled clear-sky radiance by more than 7 W/(m^2 sr). This removes the possibility of classifying thick clouds as clear sky. Thick clouds have a smooth gradient that could mimic that of a clear sky, but always emit significantly more radiance than a clear sky.

(3) Regions that are within 10 percent of the minimum detected radiance in radially symmetric regions around the zenith. For a clear sky, these rings of equal zenith angles should be constant, so this criterion will remove thin clouds that could mimic the gradient of a clear sky and would be missed by criterion (2).

An example of an image of mixed clear sky and clouds showing the detected clear sky (outlined in black) is shown in Figure 15(a) and the modeled-to-measured sky radiance regression is shown in Figure 15(b). For these data, there is a large difference between the simulated clear sky and the detected clear sky. In this example, the correction routine is able to detect the clear-sky regions and build a linear fit that is used to adjust the modeled clear-sky emission to match the measured data.

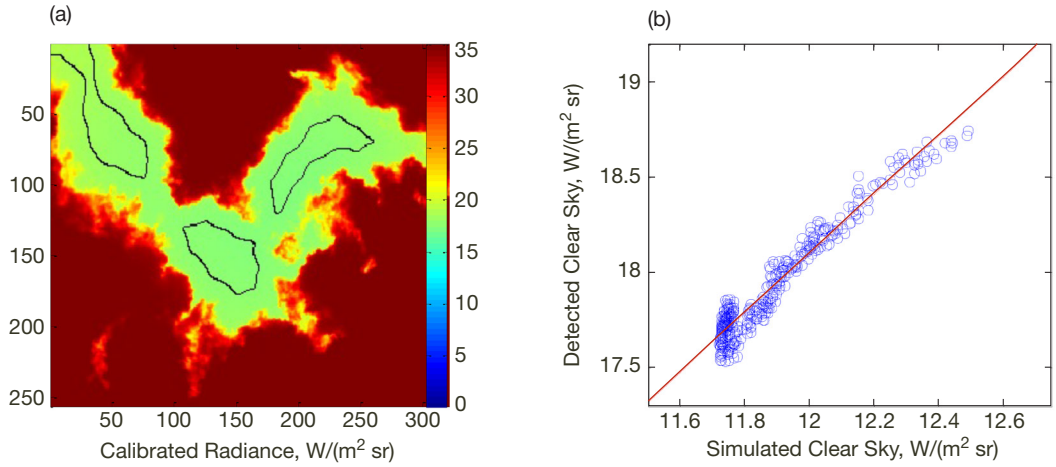

Figure 15. The gradient-based clear-sky detection is used to adjust the a priori atmospheric models to match the measured clear sky, thus reducing sensitivity to measurement errors: (a) Detected clear sky is shown as regions outlined in black; (b) the regression between the modeled and detected clear-sky radiance values.

D. Correcting the Residual Radiance Error

After removal of all errors caused by the germanium window, atmosphere, and other known sources, the ICI2 imager at TMF still exhibited a residual radiance error. This signal was not associated with clouds or other measurements, and it caused the system to report clouds erroneously during periods of clear skies. It turned out that the cause of this quasi-static residual emission was out-of-field emission from a near dome housing of the atmospheric variability monitor (AVM) at TMF. It was noted that this residual error decreased when the roof of the AVM shed was retracted and increased each time the AVM shed was brought near the ICI2. This error could be reduced in the future through mounting the ICI2 so that its top is higher than nearby sources of long-wave emission. Assuming an index of refraction of 4 for the window and 1 for air, objects located less than 15 deg above the window will experience a total reflection and will not cause scattering off the window. It is also possible that adaptive processing techniques could identify and remove per-pixel biases in the data, effectively reducing or removing this error [24].

To reduce the effect of this out-of-field scattering in the current system, a model was built to calculate and remove the error. Multiple low-radiance images that had little or no frame-to-frame differences over 15-min periods were assumed to be instances of 100 percent clear sky. For these periods, after removing the calculated atmospheric radiance, the resulting images ideally would have been zero. Instead, all these files had a positive radiance, a bias that caused the imager to erroneously report clouds during clear conditions, predominantly on one side of the image. Figure 16 shows (a) the per-pixel mean of the residual radiance for these clear-sky data files, and (b) the relationship between residual-image mean radiance and the emission of an object at the surface air temperature.

The variation throughout the year was strongly correlated with air-temperature measurements from the TMF weather station. In fact, there was found to be a linear relationship between the residual radiance error and the blackbody radiance at the air temperature. Correction routines were calculated by performing a fit to the per-pixel error and the air-

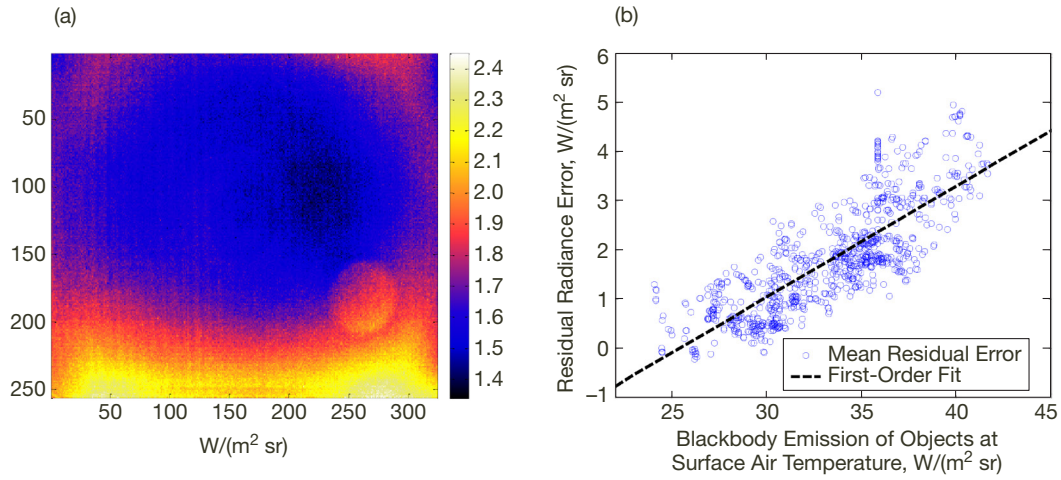

Figure 16. (a) The per-pixel mean of the residual radiance on 963 clear sky data files, and (b) the relationship between the mean radiance error and the emission of an object at the temperature of the near-surface air.

temperature blackbody radiance. This model was used to calculate and subtract the error from each image, reducing the mean error from 4 W/(m^2 sr) to 0.5 W/(m^2 sr). Despite the improvement, the remaining error does have an impact on the sensitivity to thin clouds. These results will be discussed further in Section IV.

E. Cloud Detection and Classification

The ICI2 is able to detect the presence of clouds in the sky, but in addition to simple cloud presence detection, the cloud-detection algorithms developed for the ICI2 classify thin clouds according to their visible-wavelength optical depth (OD) or the optical attenuation loss in decibels at or near a wavelength of 550 nm. Two aspects of cirrus clouds enable this association of LWIR emission to cloud OD or attenuation. First, the occurrence of cirrus clouds of higher OD decreases with increasing cloud-base altitude [25]. Second, there is a relationship between cloud OD and cloud emissivity in the LWIR, which can be used to predict increasing cloud emissivity with increasing OD [26,27]. Finally, the relative spectral flatness of cloud optical properties allows this attenuation value to be applied at wavelengths throughout the visible and near-infrared spectrum (such as optical communication wavelengths near and beyond 1 μm) [28].

In the ICI2 data processing, clouds are classified typically into six different categories by a multilevel threshold after atmosphere emission removal [12]. To develop these thresholds, simulations were run using MODTRAN software. In these simulations, the atmosphere at TMF was modeled with radiosonde measurement data. Concerning cloud simulations in MODTRAN, cloud models used cloud height (base and top) and cloud optical depth information from the database at the Atmospheric Radiation Measurement site located at Lamont, Oklahoma [29]. The resulting simulations were processed to provide a variety of cloud emission thresholds selected to correspond with specific values of fading in dB, as summarized in Table 1. To account for seasonable variability, unique thresholds were calculated for each month of the year (Table 2).

Table 1. Optical depth and attenuation for the ICI2.

Threshold Number	Cloud Attenuation, dB	Cloud Optical Depth
1	Clear sky (~0)	~0
2	<1	<0.2304
3	<2	<0.4608
4	<4	<0.9217
5	<8	<1.8433
6	<12	<2.7650
7	≥12	≥2.7650

Table 2. Calculated threshold levels for the ICI2 throughout the year in W/(m^2 sr).

Level	dB	Jan	Feb	Mar	Apr	May	Jun	Jul	Aug	Sep	Oct	Nov	Dec
1	Clear	0.48	0.60	0.57	0.56	0.57	0.61	0.62	0.64	0.57	0.58	0.54	0.58
2	<1	1.21	1.20	1.15	1.16	1.17	1.23	1.25	1.26	1.27	1.33	1.13	1.21
3	<2	2.57	2.55	2.53	2.58	2.54	2.80	2.52	2.85	2.9	2.80	2.59	2.60
4	<4	4.11	4.02	3.8	3.99	4.06	4.40	4.74	4.75	4.54	4.46	4.09	4.10
5	<8	7.4	8.9	9.24	9.42	10.3	11.25	11.66	11.54	10.81	10.43	10.24	9.57
6	<12	15.12	15.3	14.74	14.88	16.16	17.41	17.00	17.30	16.45	16.08	15.83	15.03
7	≥12												

These thresholds define regions where 95 percent of the clouds had OD or dB attenuation less than a specified value. This technique, therefore, bins clouds by the maximum expected OD or dB attenuation. All clouds with radiance greater than threshold 6 are classified as level 7. For example, based on the January model, 95 percent of the clouds with emission between 0.48 W/(m^2 sr) and 1.21 W/(m^2 sr) have OD up to 0.23, or optical attenuation up to 1 dB. Similarly, 95 percent of the clouds with emission between 1.21 and 2.57 W/(m^2 sr) have OD up to 0.46 or an attenuation up to 2 dB. The monthly clear-sky thresholds correspond to a maximum cloud optical attenuation of 0.25 dB.

F. Spatial Biases in the Data

Even after correction for the radiance bias described in Section III.D, there is still an increase of approximately 0.5 W/(m^2 sr) along the bottom of the image. This error biases thin-cloud detection, causing an average increase of 0.9 dB along the bottom half of the image. Figure 17(a) shows the average cloud attenuation for the entire TMF data set, clearly indicating the residual bias along and near the bottom edge of the image. To study the effect of this bias, the data were split into two regions and reanalyzed; Figure 17(b) shows the mask that was used to split the data into the red region with a bias and the blue region without a bias.

This reanalysis found differences of 9.6 percent in the thin-cloud detection (dB <2) between the masked and unmasked regions. For the thicker clouds, this difference decreases, and is less than 0.5 percent for clouds with attenuation greater than 4 dB. Overall, there is an

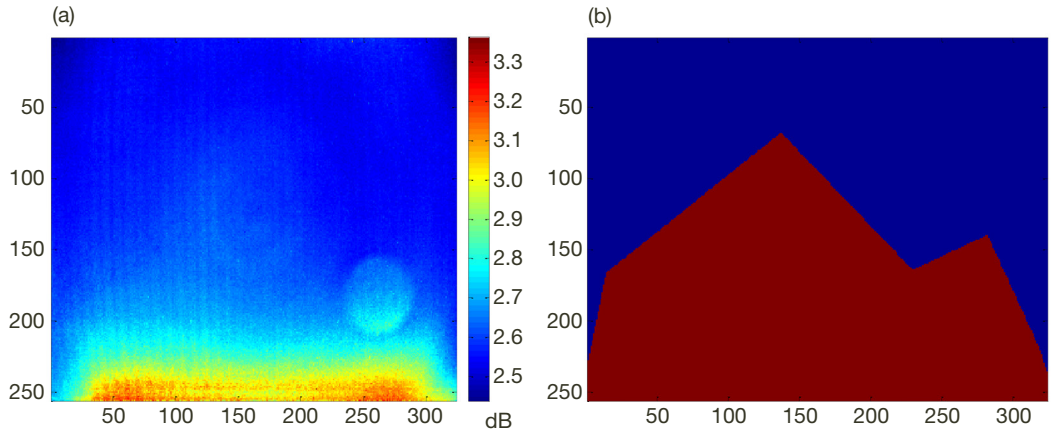

Figure 17. The region in red represents the pixels of the detector where a significant bias is expected (masked), and the regions in blue are the pixels where no bias is expected (unmasked).

11.0 percent difference in the total detected cloud amount between the biased and unbiased sides of the image. Table 3 shows this difference at each threshold (recall that this bias can be removed with proper instrument mounting).

Table 3. Difference by threshold.

Threshold Number	Cloud Attenuation, dB	Cloud Fraction Percent Difference
1	Clear sky	11
2	1	6.78
3	2	3.27
4	4	0.47
5	8	0.23
6	12	–0.02
7	>12	0.26

IV. Cloud Data Processing

This section presents examples of data derived from the measurements obtained during two years of the ICI2 deployment at TMF. These data were selected to show a variety of different sky conditions measured during day and night, and have been processed following the procedure outlined in Section III.

A. Cloud Spatial Analysis

This section presents processed cloud data as two-panel figures (Figures 18–21), for which the left panel is the calibrated sky radiance and the right panel is the cloud attenuation. Cloud attenuation is referred in the wavelength range from the visible to the near-infrared. The figures cover the full spectrum of cloud types: clear sky in Figure 18; thin cirrus clouds in Figure 19; thick clouds in Figure 20; and mixed thin and thick clouds in Figure 21.

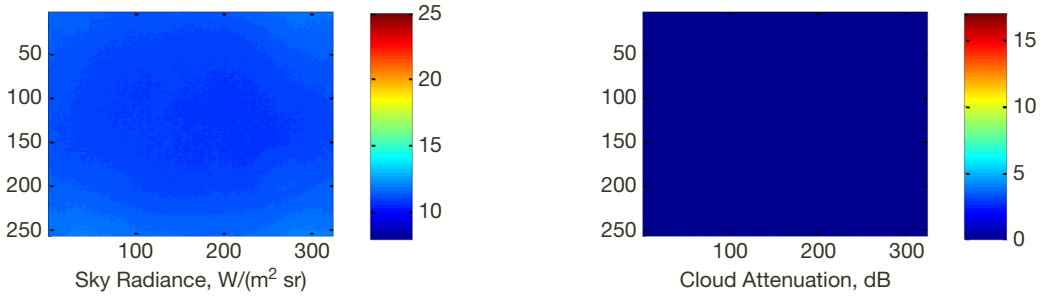

Figure 18. Clear sky detected on July 21, 2008, at 19:24 UTC.

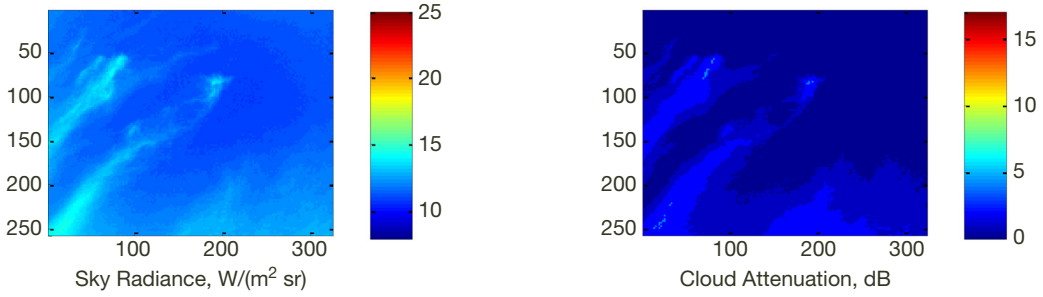

Figure 19. Optically thin cirrus clouds detected on June 11, 2009, at 18:44 UTC.

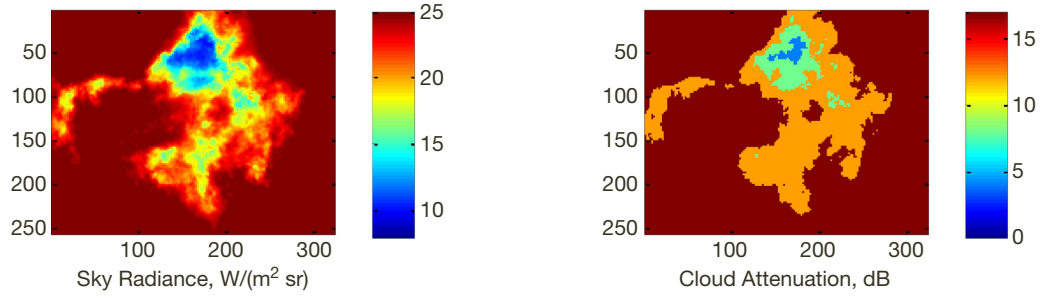

Figure 20. Optically thick clouds detected on February 8, 2010, at 16:44 UTC.

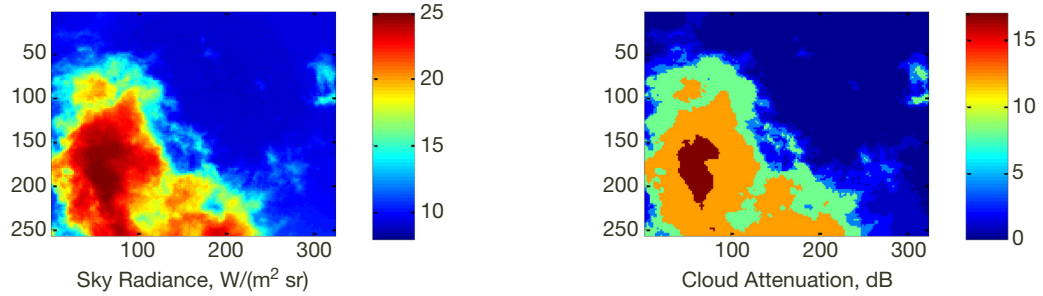

Figure 21. Mixed optically thin and thick clouds on April 30, 2010, at 09:46 UTC.

B. Cloud Temporal Analysis

In addition to providing spatial maps of clouds, the ICI2 images can be used to determine a value of total cloud amount for analysis as a time series. Total cloud amount is the percentage of cloudy pixels across the entire image. Using a multivalue cloud threshold, the cloud amount data can be separated by cloud attenuation levels in each pixel of the sensor array.

Figures 22 and 23 show the measured cloud amount for two 48-hr periods. Figure 22 shows data collected from February 13–15, 2009, and Figure 23 shows data from December 3–5, 2009. During both periods, the sky starts out largely clear, the cloud amount rapidly increases, and the sky becomes overcast. Notice that even though the patterns of total cloud amount are similar, the compositions of these clouds are different. During the period of February 13–15, 2009, the increase in cloud amount was caused by thick clouds with attenuation greater than 12 dB. However, during the period of December 3–5, 2009, the clouds were primarily thin, with an average attenuation between 2 dB and 5 dB. The importance of this capacity of characterizing cloud optical loss in real time by the ICI2 system is made evident by considering an operational scenario. In an optical communication scenario, the impairments caused by these two periods of similar cloud amount would be very different. With sufficient link margin, communication would have been possible through the low-attenuation December clouds (Figure 23), while communication would not have been possible through the more highly attenuating February clouds (Figure 22).

C. Long-Term Cloud Statistics: Large FOV

In this section, we show the cloud amount measured by the ICI2 system at TMF for the full two-year deployment period. Because of the bias described in the previous section, the cloud statistics shown here use only the unbiased data. For these data, the cloud images were first averaged spatially to represent the average cloud amount across the unbiased region of the imager's field of view, and then were averaged temporally over a given set of consecutive samples. These data are presented with one-week temporal averaging in Figure 24 and with one-month temporal averaging Figure 25. In these figures, the clear-sky amount is one minus the cloud amount and therefore is represented by the white space above the bars representing cloud amount.

These figures show that cloud amount at TMF tends to increase during the winter, with a peak of 51 percent in February, during which time over 60 percent of the clouds have high attenuation. During May–October, there is minimal cloud amount (approximately 22 percent), excluding a peak of 36.5 percent in June. These months experience primarily optically thin clouds with attenuation less than 8 dB.

Average annual cloud amount at TMF during this deployment was 30.6 percent. Of these clouds, 46.3 percent were optically thin with attenuation less than 2 dB, 18.3 percent had attenuation between 2 and 12 dB, and 35.4 percent were optically thick with attenuation greater than 12 dB. Table 4 shows the cloud amount by month at TMF. Table 5 presents the fraction of clouds detected in each classification level.

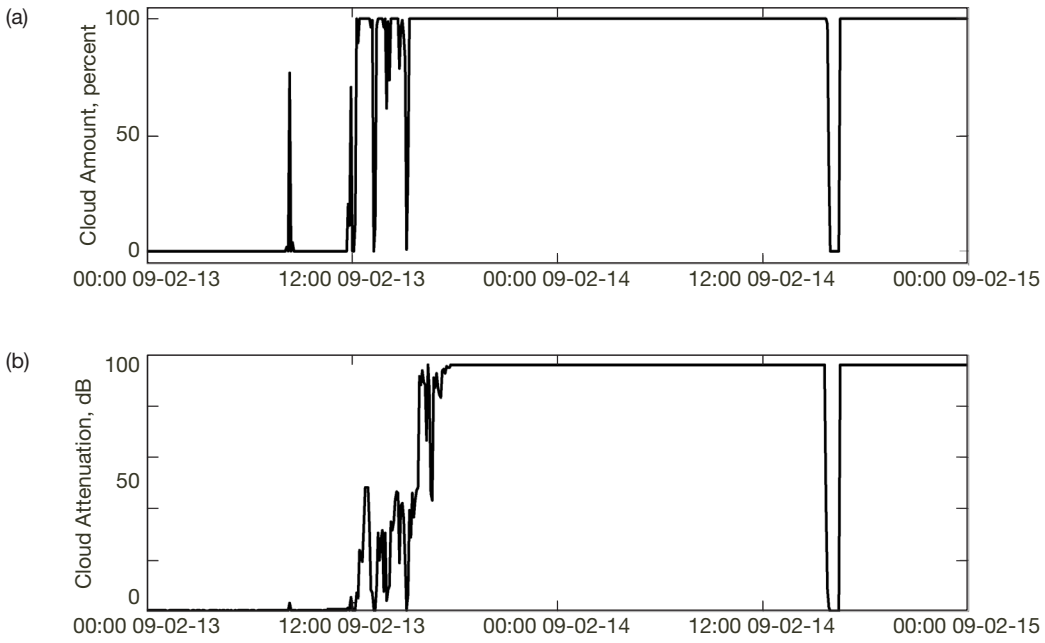

Figure 22. (a) Average cloud amount, and (b) cloud attenuation for February 13–15, 2009. The sky starts out clear, but clouds move in near mid-day on February 13 and the sky becomes completely overcast. The cloud classification algorithm shows that these were optically thick clouds with high attenuation.

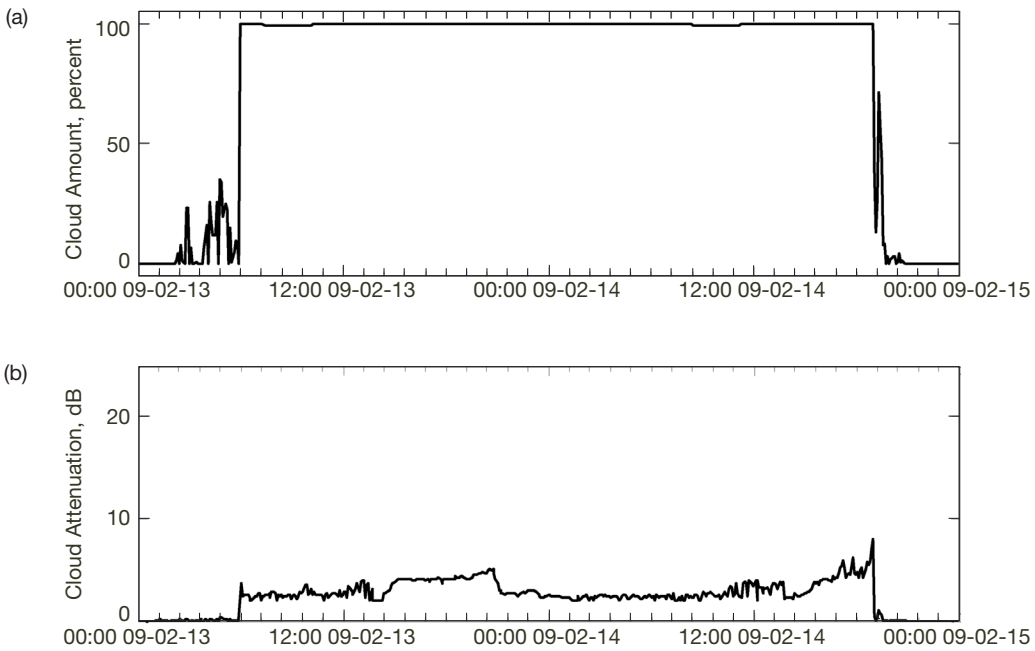

Figure 23. (a) Average cloud amount, and (b) cloud attenuation for December 3–5, 2009. The sky starts out clear and later becomes overcast. The cloud attenuation data show that these clouds had low attenuation and some level of optical communication may have been possible.

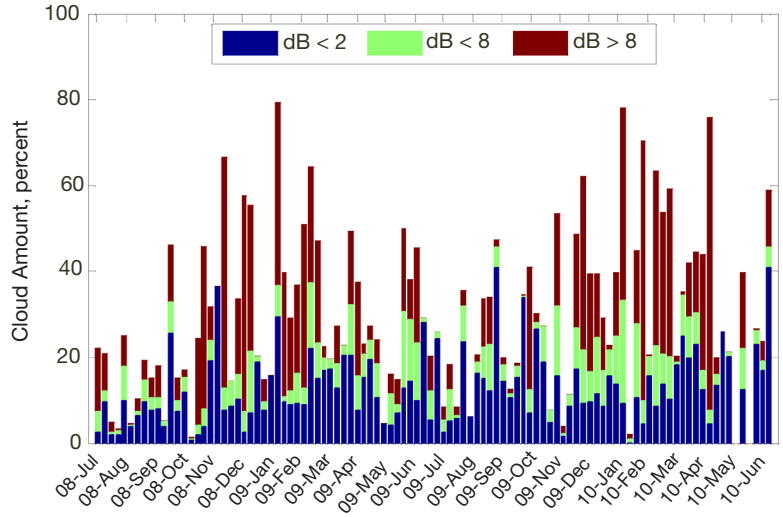

Figure 24. Average weekly cloud amount over the full two-year experiment.

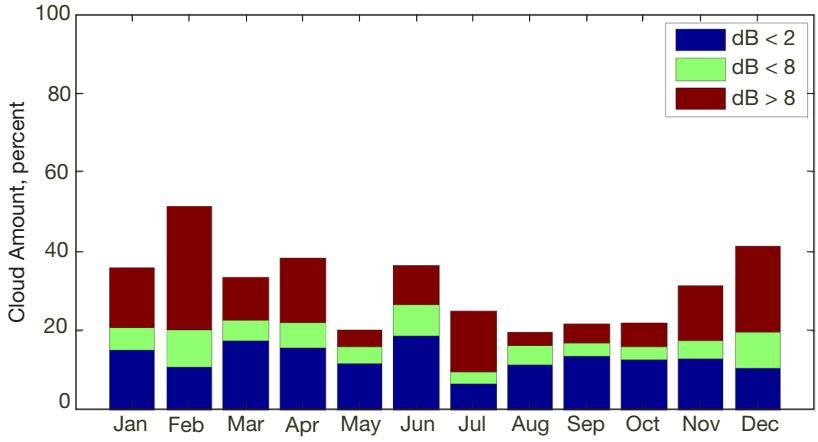

Figure 25. Average monthly cloud amount over the full two-year experiment.

Table 4. Average monthly cloud amount measured by the ICI2, percent.

	Jan	Feb	Mar	Apr	May	Jun	Jul	Aug	Sep	Oct	Nov	Dec
Clear	64.2	48.6	66.6	61.6	79.9	63.5	74.9	80.4	78.3	78.1	68.7	58.6
Cloudy	35.8	51.4	33.4	38.4	20.1	36.5	25.1	19.6	21.7	21.9	31.3	41.4

Table 5. Cloud amount by cloud type, percent.

dB	Jan	Feb	Mar	Apr	May	Jun	Jul	Aug	Sep	Oct	Nov	Dec
Clear	64.2	48.6	66.6	61.6	79.9	63.5	74.9	80.4	78.3	78.1	68.7	58.6
1	10.9	6	8.9	8.9	6.1	9.6	3.9	5.5	9.2	10.0	9.0	5.3
2	3.9	4.9	8.5	6.8	5.7	9.2	2.5	6.0	4.3	2.5	3.8	5.2
4	2.0	3.0	2.0	2.3	1.1	2.6	0.8	1.5	1.1	1.1	1.3	3.1
8	3.7	6.2	3.3	3.9	3.0	5.3	2.1	3.1	2.3	2.2	3.4	5.8
12	5.2	6.2	1.6	2.4	2.7	6.2	3.3	2.23	3.3	1.6	1.9	4.9
>12	10.0	25.2	9.2	14.1	1.6	3.7	12.5	1.3	1.5	4.5	12.0	17.1

D. Statistics of Duration of Clear and Cloudy Skies: Large FOV

The long-term data set at TMF allowed for calculation of statistics of clear and cloudy sky durations. To make these calculations, the duration of clear and cloudy skies was observed for the 729 calendar days of data, from July 15, 2008 to July 14, 2010. Time periods that included an instrument startup or shutdown were omitted (shutdown or power-up events were determined by gaps between data points exceeding 30 min. Omitting such data ensured that only periods that were fully observed were used in the statistics. Overall, 62.4 percent of the data were clear skies (defined as the sky being 90 percent or greater cloud free) and 37.6 percent were cloudy (defined as the sky being 10 percent cloudy or more). The duration of the time periods used in this study, along with their numbers of occurrence, are shown on a logarithmic plot in Figure 26: (a) cloudy periods, (b) clear-sky periods.

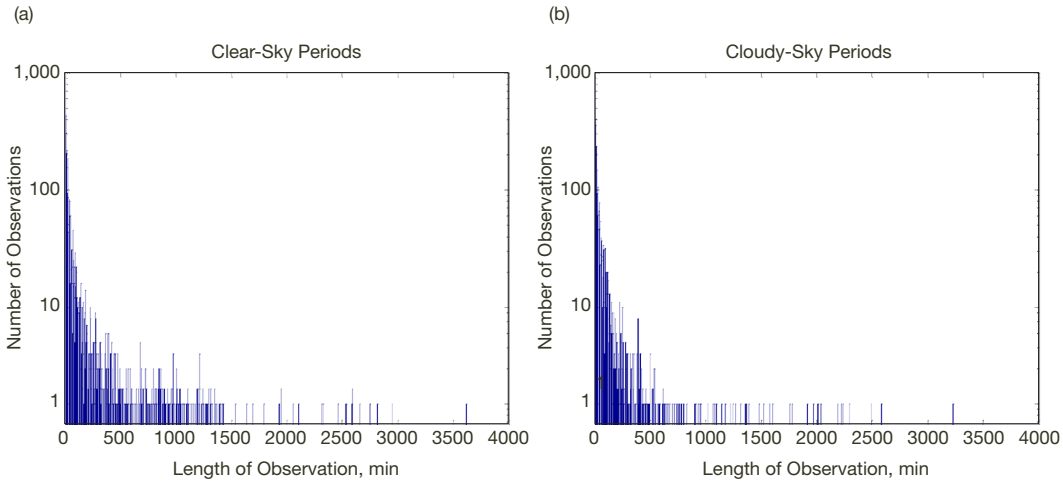

Figure 26. Number of occurrence by duration of clear and cloudy periods in 1-min increments, measured with a 62-deg FOV imager: (a) clear sky observations, and (b) cloudy sky observations.

The analysis of these data shows a nearly equal frequency of occurrence of cloudy and clear skies, except for the longest durations exceeding 10 hr (600 min). Above these time lengths, the sky was observed to be primarily clear. This suggests that at TMF, periods of clear skies and cloudy skies have nearly the same frequency of occurrence for short durations. However, it is more common for long periods of clear skies to occur than long periods of cloudy skies.

Figure 27 presents the same data as Figure 26, now binned and scaled by the observation length to represent the observation length versus the percent of total observed time. From this figure, it is easier to see the strong contribution that long periods (greater than approximately 16.7 hr or 1000 min) have on the total observed cloud amount. It is interesting to note that the contributions of clear and cloudy skies are quite similar except in the region from 5 to 33 hr (300 to 2000 min), which accounts for nearly 40 percent of the observations made at the TMF. Furthermore, Figure 27 shows that the most commonly observed atmospheric condition over the TMF is clear sky with a period of approximately 24 hr (1440 min).

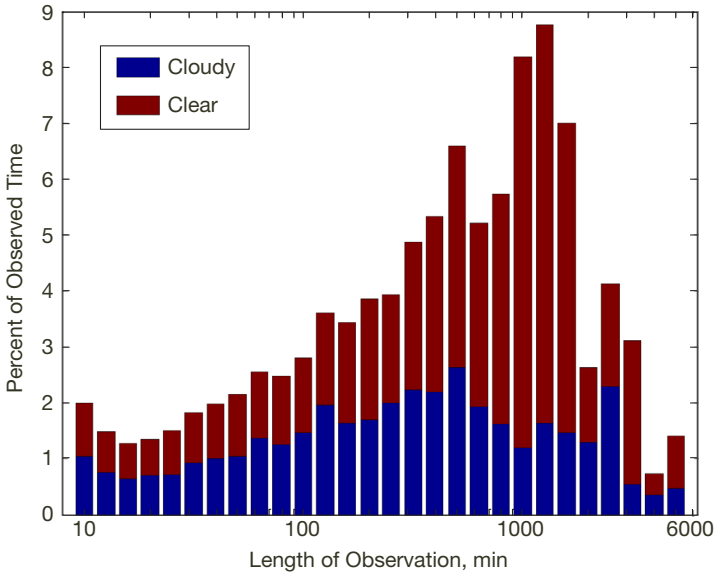

Figure 27. Probability density function of the sky remaining in an unchanged clear (red) or cloudy (blue) state, measured with a 62-deg FOV.

E. Narrow FOV Cloud Statistics

The cloud statistics presented in the previous subsection used the ICI2 full FOV (measured to be 62 deg along the diagonal). In a number of applications, including space-to-ground optical communications, one may be interested in characterizing the cloud coverage over a much smaller FOV in the sky. To do such an analysis, cloud cover statistics were calculated over a reduced FOV, namely, 1 deg centered at the zenith.

The first data product to be calculated for this reduced FOV was the cumulative distribution function (CDF) of cloud attenuation (Figure 28). According to the reported data, the sky is cloud free 62.5 percent of the time for a 1-deg FOV and 62.4 percent of the time for the full 62-deg diagonal FOV.

Next, the statistics of the duration of clear sky and cloudy sky were calculated for the 1-deg FOV (Figures 29 and 30). A comparison of the results in Figures 26 and 27 shows that there are great similarities between the statistics collected over the imager's whole 62-deg FOV and the 1-deg FOV. This result may be very surprising; however, it may be explained by Taylor's hypothesis, which states that the covariance in time is related to the covariance in space by the mean flow velocity when the turbulence is small compared to the mean flow [9,30]. Therefore, under these conditions when Taylor's hypothesis is found to be valid, the cloud amount statistics for a large sky region can be estimated accurately over periods of minutes to hours from cloud amount statistics for a small sky region. However, it has been shown that over a period of about 1 hr, Taylor's hypothesis tends to fail under conditions dominated by high cirrus (non-boundary-layer clouds), changing wind speed or direction, rapidly developing or dissipating clouds, and multiple cloud layers [30]. It is particularly interesting to note that in the data presented in Figures 27 and 30, the narrow- and wide-angle probability density functions are most different near an observation

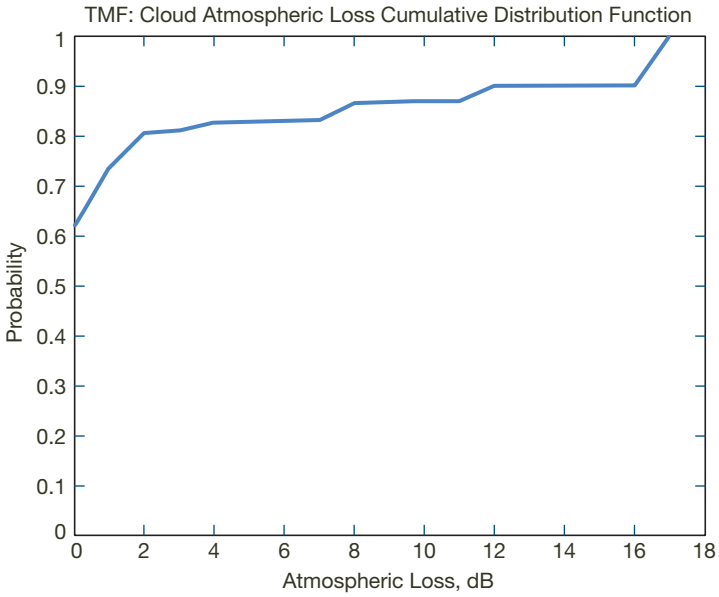

Figure 28. Cumulative distribution function (CDF) of attenuation measured in 1-deg FOV.

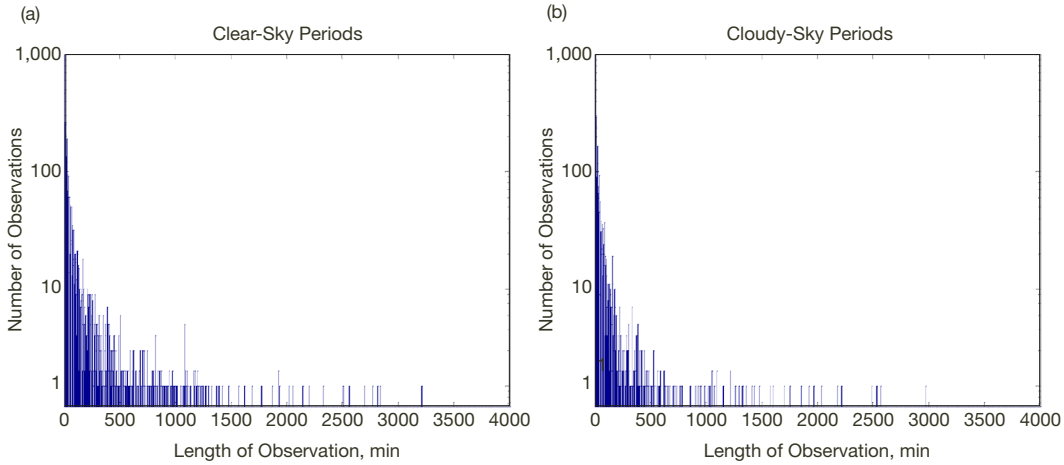

Figure 29. Number of occurrences by duration of clear and cloudy periods in 1-min increments, measured with 1-deg FOV: (a) clear sky observations and (b) cloudy sky observations.

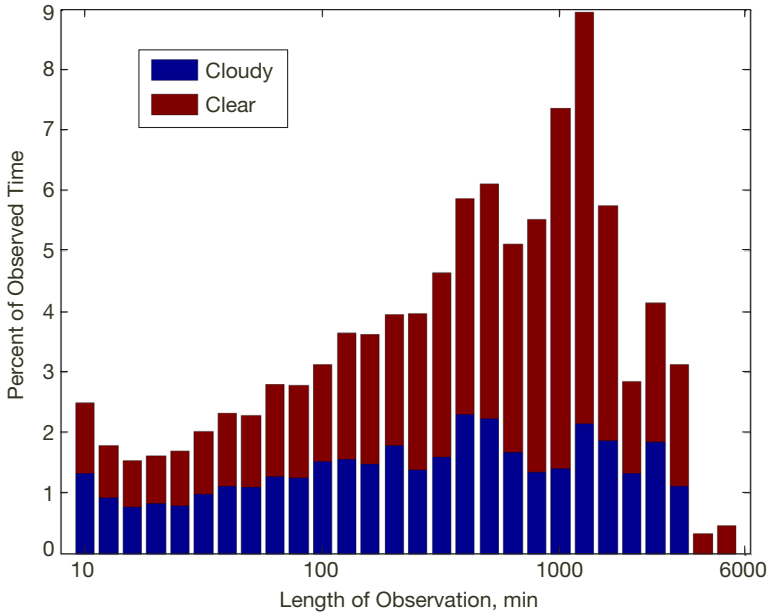

Figure 30. Probability density function of the sky remaining in an unchanged clear (red) or cloudy (blue) state, measured with a 1-deg FOV.

length of approximately 600–700 min, or 10–12 hr. This could suggest that there is diurnal (day–night) cloud variability in the wide-angle images that is not fully represented by the narrow-angle data.

It is unknown whether or not Taylor's hypothesis can be applied to longer-term cloud statistics, and therefore it is unknown how narrow-angle and wide-angle cloud statistics compare in long observational data sets. Consequently, the ICI2 data presented here enable unprecedented studies of cloud statistics, with particular relevance to the narrow beams that are used at widely varying pointing angles in free-space optical communications. For example, ICI2 data could be used to determine the effect of measured cloud fields on an optical beam that is moving as it tracks a low-Earth-orbit satellite.

V. Comparisons with the TMF Sun Photometer

A level of validation of the ICI2 processing routines is possible through a comparison with the cloud-screened Sun photometer data (named level 2.0) available at TMF. As a Sun-staring system, the Sun photometer only operates during the day and is impeded by the presence of thick clouds along the sensor-to-Sun path. The level 2.0 data have been screened for the presence of clouds and have had any suspected cloudy data removed. Thus, it was hypothesized that the ICI2 should report clear sky or low cloud attenuations when the Sun photometer reported level 2.0 data.

Level 2.0 cloud-screened Sun photometer data from TMF were available for the full ICI2 deployment period under consideration. ICI2 data were analyzed for times within 5 min of when the Sun photometer reported level 2.0 data. For these times, the ICI2 reported average

cloud attenuation of 0.38 dB, cloud-free sky 74.2 percent of the time, and an average attenuation lower than 2 dB 92.7 percent of the time. Thus, the ICI2 showed very low average cloud attenuation during periods of level 2.0 Sun photometer operation (e.g., when there were no clouds in the Sun photometer's FOV). During these times, when the ICI2 did report clouds they were primarily thin cirrus, with attenuation less than 2 dB.

Figure 31 shows the monthly probability that both the ICI2 and the Sun photometer reported clear skies simultaneously, binned and averaged by month. It is important to note that during the month of August, the ICI and Sun photometer never reported data within 5 min of each other, so the August data therefore represent missing data, and not a lack of accuracy.

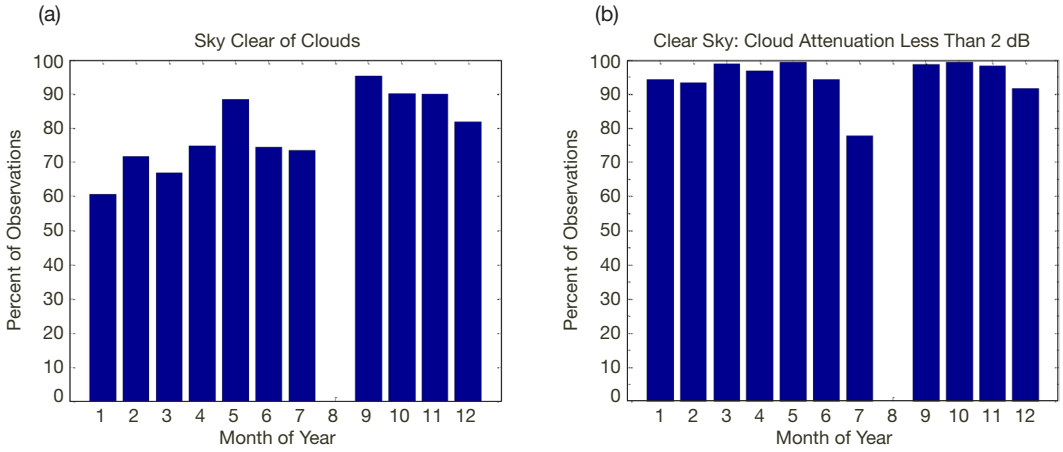

Figure 31. Monthly probability that the 62-deg FOV ICI2 and Sun photometer reported clear skies simultaneously: (a) Sun photometer and ICI clear sky; (b) Sun photometer clear sky and ICI cloud attenuation less than 2 dB. There were no simultaneous observations in August.

These observations agree with what is expected, since thicker clouds would obscure the Sun photometer's view of the Sun, preventing it from collecting data. During periods when the Sun photometer had an unobstructed view of the Sun, ICI2 data show that if clouds were detected, they tended to be thin cirrus clouds. This agrees with the hypothesis that the ICI2 should report clear sky or low cloud attenuation when the Sun photometer was able to make measurements, which tends to validate the accuracy of the ICI system.

VI. Conclusions

A cloud imaging system has been developed and deployed at the NASA/JPL Table Mountain Facility to measure spatial and temporal cloud patterns and characteristics. This cloud imaging system is a small, compact, and relatively low-cost thermal infrared cloud imager that can be redeployed easily at different locations and can be reproduced with reasonably low cost.

The cloud imaging system operated (and it is still operating up to date) almost continuously for two years with minimal assistance from on-site technicians, and demonstrated its ability

to run reliably outdoors. This system is capable of collecting high-spatial-resolution and high-temporal-resolution statistics of cloud presence. An important feature of this system is the classification of clouds by their optical attenuation, which is of great interest for possible operating scenarios involving optical communication through thin clouds. The system measures long-wavelength infrared cloud radiance and from it retrieves the cloud optical depth in the visible–near-infrared spectral region.

Cloud statistics calculated from data collected during the deployment at the TMF site pointed out a significant seasonal variability in detected cloud cover. During this deployment, the cloud statistics were very similar for either the entire field of view or a narrow 1-deg field of view. Cloud amount increased during the winter with a peak in February, during which over 50 percent of the clouds had high attenuation. There is a noticeable increase in cloud cover during June but these clouds are primarily thin clouds that would produce less than 2 dB of attenuation. The 1-deg field of view was determined to be cloud free 62.5 percent of the time.

Considering the cloud coverage temporal dynamics, the analysis of these data also showed that the occurrence of long cloud-free periods is much more likely than that of long cloudy periods. This is most distinct for time periods of length between 5 hr to 33 hr, which collectively account for nearly 40 percent of the observations made at TMF.

Work is ongoing to improve the abilities of the cloud imaging systems. The atmospheric emission removal algorithms are being refined, along with the cloud OD calculations. These refinements will further improve the accuracy of these systems, resulting in better cloud detection, especially detection of thin cirrus. Finally, improved cloud imaging systems are under development, including a large-FOV cloud imager that is already deployed at the NASA/JPL Deep Space Network Communications Complex at Goldstone, California.

Acknowledgment

The authors would like to thank Dr. Stephen Slobin for helpful review comments that improved the manuscript.

References

[1] H. Hemmati, *Near Earth Laser Communications*, Boca Raton, Florida: CRC Press, 2009.

[2] H. Hemmati, *Deep Space Optical Communications*, Hoboken, New Jersey: Wiley Press, 2006.

[3] S. Piazzolla, S. Slobin, and P. E. Amini, *Cloud Coverage Diversity Statistics for Optical Communications in the Southwestern United States*, NASA JPL Publication 00-13, Pasadena, California: Jet Propulsion Laboratory, California Institute of Technology, 2000.

[4] D. M. Boroson, J. J. Scozzafava, D. V. Murphy, B. S. Robinson, and H. Shaw, "The Lunar Laser Communications Demonstration (LLCD)," *Proceedings, Third IEEE International Conference on Space Mission Challenges for Information Technology*, Pasadena, California, July 29–23, 2009.

[5] B. Edwards, D. Israel, K. Wilson, J. Moores, and A. S. Fletcher, "The Laser Communications Relay Demonstration," International Conference on Space Optics, Ajaccio, Corsica, October 9–12, 2012.

[6] J. H. Churnside and K. Shaik, *Atmospheric Propagation Issues Relevant to Optical Communications*, NOAA Technical Memorandum ERL WPL-159, 1989.

[7] G. S. Wojcik, H. L. Szymczak, R. J. Alliss, R. P. Link, M. E. Craddock, and M. L. Mason, "Deep-space to Ground Laser Communications in a Cloudy World," *Proceedings of 5892, Free-Space Laser Communications V*, 589203-1–11, San Diego, California, July 31, 2005.

[8] K. E. Wilson, N. Page, J. Wu, and M. Srinivasan, "The JPL Optical Communications Telescope Laboratory Test Bed for the Future Optical Deep Space Network," *The Interplanetary Network Progress Report*, vol. 42-153, Jet Propulsion Laboratory, Pasadena, California, pp. 1–12, May 15, 2003.
http://ipnpr.jpl.nasa.gov/progress_report/42-153/153G.pdf

[9] B. Thurairajah and J. A. Shaw, "Cloud Statistics Measured with the Infrared Cloud Imager (ICI)," *IEEE Transactions on Geoscience and Remote Sensing*, vol. 43, no. 9, pp. 2000–2007, September 2005.

[10] J. A. Shaw, P. W. Nugent, N. J. Pust, and B. Thurairajah, "Radiometric Cloud Imaging With an Uncooled Microbolometer Thermal Infrared Camera," *Optics Express*, vol. 13, no. 15, pp. 5807–5817, 2005.

[11] P. W. Nugent, "Wide-Angle Infrared Cloud Imaging for Cloud Cover Statistics," Masters Thesis, Electrical Engineering Montana State University, Bozeman, Montana, January 2008.
http://etd.lib.montana.edu/etd/2008/nugent/NugentP0508.pdf

[12] P. W. Nugent, J. A. Shaw, and S. Piazzolla, "Infrared Cloud Imaging in Support of Earth–Space Optical Communication," *Optics Express*, vol. 17, no. 10, pp. 7862–7877, 2009.

[13] S. Platnick, M. D. King, S. A. Ackerman, W. P. Menzel, B. A. Baum, J. C. Riédi, and R. A. Frey, "The MODIS Cloud Products: Algorithms and Examples From Terra," *IEEE Transactions on Geoscience and Remote Sensing*, vol. 41, no. 2, pp. 459–473, February 2003.

[14] G. L. Stephens, D. G. Vane, R. J. Boain, G. G. Mace, K. Sassen, Z. Wang, A. J. Illingworth, E. J. O'Connor, W. B. Rossow, S. L. Durden, S. D. Miller, R. T. Austin, A. Benedetti, C. Mitrescu, and the CloudSat Science Team, "The CloudSat Mission and the A-Train," *Bulletin of the American Meteorological Society*, vol. 83, no. 12, pp. 1771–1790, December 2002.

[15] C. N. Long, D. W. Slater, and T. Tooman, *Total Sky Imager (TSI) Model 880 Status and Testing Results*, U.S. Department of Energy, Washington, D.C., ARM Technical Report ARM TR-006, November 2001.
http://www.arm.gov/publications/tech-reports

[16] J. E. Shields, M. E. Karr, T. P. Tooman, D. H. Sowle, and S. T. Moore, "The Whole Sky Imager — A Year of Progress," *Proceedings of the 8th Atmospheric Radiation Measurement (ARM) Science Team Meeting*, pp. 677–685, Tucson, Arizona, March 1998.

[17] P. W. Nugent, J. A. Shaw, and S. Piazzolla, "Wide-Angle Infrared Cloud Imaging for Measuring Cloud Statistics in Support of Earth–Space Optical Communication," *Proceedings of SPIE 6709, Free-Space Laser Communications VII*, pp. 6709F1–9, San Diego, California, August 26, 2007.

[18] P. W. Nugent, J. A. Shaw, N. J. Pust, and S. Piazzolla, "Correcting Calibrated Sky Imagery for the Effect of an Infrared Window," *Journal of Atmospheric and Oceanic Technology*, vol. 26, no. 11, pp. 2403–2412, November 2009.

[19] G. P. Anderson, S. A. Clough, F. X. Kneizys, J. H. Chetwynd, and E. P. Shettle, "AFGL Atmospheric Constituent Profiles (0–120 km)," Air Force Geophysics Laboratory, Environmental Research Papers, no. 954, 1986.

[20] G. P. Anderson, A. Berk, P. K. Acharya, M. W. Matthew, L. S. Bernstein, J. H. Chetwynd, H. Dothe, S. M. Adler-Golden, A. J. Ratkowski, G. W. Felde, J. A. Gardner, M. L. Hoke, S. C. Richtsmeier, B. Pukall, J. Mello, and L. S. Jeong, "MODTRAN4: Radiative Transfer Modeling for Remote Sensing," *Proceedings of SPIE 3866*, pp. 2–10, 1999.

[21] B. N. Holben, T. F. Eck, I. Slutsker, D. Tanré, J. P. Buis, A. Setzer, E. Vermote, J. A. Reagan, Y. J. Kaufman, T. Nakajima, F. Lavenu, I. Jankowiak, and A. Smirnov, "AERONET — A Federated Instrument Network and Data Archive for Aerosol Characterization," *Remote Sensing of Environment*, vol. 66, no. 1, pp. 1–16, October 1998.

[22] C. H. Reitan, "Surface Dew Point and Water Vapor Aloft," *Journal of Applied Meteorology*, vol. 2, no. 6, pp. 776–779, December 1963.

[23] C. Tomasi, "Determination of the Total Precipitable Water Vapor by Varying the Intercept in Reitan's Relationship," *Journal of Applied Meteorology*, vol. 20, no. 9, pp. 1058–1069, September 1981.

[24] B. M. Ratliffe, M. M. Hayat, and J. S. Tyo, "Algorithm for Radiometrically-Accurate Nonuniformity Correction with Arbitrary Scene Motion," *Proceedings of SPIE 5076, Infrared Imaging Systems: Design, Analysis, Modeling, and Testing XIV*, pp. 82–91, Orlando, Florida, April 21, 2003.

[25] D. K. Lynch, K. Sassen, D. O'C. Starr, and G. Stephens (eds.), *Cirrus*, New York: Oxford University Press, 2002.

[26] Q. Fu and K. N. Liou, "Parameterization of the Radiative Properties of Cirrus Clouds," *Journal of the Atmospheric Sciences*, vol. 50, no. 13, pp. 2008–2025, July 1993.

[27] K. Sassen and G. G. Mace, "Ground-Based Remote Sensing of Cirrus Clouds," in *Cirrus*, D. K. Lynch, K. Sassen, D. O'C. Starr, and G. Stephens (eds.), pp. 168–209, New York: Oxford University Press, 2002.

[28] J. A. Reagan, X. Wang, and M. T. Osborn, "Spaceborne Lidar Calibration from Cirrus and Molecular Backscatter Returns," *IEEE Transactions on Geoscience and Remote Sensing*, vol. 40, no. 10, pp. 2285–2290, October 2002.

[29] J. E. M. Goldsmith, F. H. Blair, S. E. Bisson, and D. D. Turner, "Turn-key Raman Lidar for Profiling Atmospheric Water Vapor, Clouds, and Aerosols," *Applied Optics*, vol. 37, no. 21, pp. 4979–4990, July 20, 1998.

[30] C.-H. Sun and L. R. Thorne, "Inferring Spatial Cloud Statistics from Limited Field-of-View, Zenith Observations," *Proceedings of the 5th Atmospheric Radiation Measurements (ARM) Science Team Meeting*, pp. 331–334, San Diego, California, March 1995. http://www.arm.gov/publications/proceedings/conf05